Final Draft

of the original manuscript

Yang, H.; Huang, Y.; Tolnai, D.; Kainer, K.U.; Dieringa, H.:

Influences of Al and high shearing dispersion technique on the microstructure and creep resistance of Mg-2.85Nd-0.92Gd-0.41Zr-0.29Zn alloy.

In: Materials Science and Engineering A. Vol. 764 (2019) 138215
First published online by Elsevier: 26.07.2019

https://dx.doi.org/10.1016/j.msea.2019.138215

Influences of Al and high shearing dispersion technique on the microstructure and creep resistance of Mg-2.85Nd-0.92Gd-0.41Zr-0.29Zn alloy

Hong Yang*, Yuanding Huang, Domonkos Tolnai, Karl Ulrich Kainer, Hajo Dieringa

MagIC, Magnesium Innovation Centre, Helmholtz-Zentrum Geesthacht, Max-Planck-Straße 1, 21502 Geesthacht, Germany

*E-mail: hong.yang@hzg.de

Abstract

Effects of 0.25% Al addition and the high shearing dispersion technique (HSDT) on the microstructure and creep resistance of Mg-2.85Nd-0.92Gd-0.41Zr-0.29Zn (Elektron21, El21) alloy were investigated. Compressive creep testes were performed at 240 °C over a stress range between 80-140 MPa. The results indicate that the creep resistance of El21 was significantly improved by about one order of magnitude with the addition of 0.25% Al and HSDT than that of El21 without Al and HSDT. Microstructural characterizations show that the grains were coarsened from 80.1±5.0 to 167.0±5.7 μm due to the loss of grain refiner Zr by the chemical reaction of Al with Zr. With the addition of 0.25% Al to El21, the grain morphology was changed from equiaxed to typical dendrite. The morphology of intermetallic Mg_3RE was modified from network to a pronounced dendritic structure. Owing to the employment of HSDT, the dendrite arm spacing of primary α-Mg was refined from 74.0±6.4 to 56.2±1.6 μm in Al-containing El21 alloy, the dominant Al-Zr compound changed from Al_2Zr_3 to Al_2Zr phase. A small amount of Al_2Nd phase was formed. Creep data analysis indicates that the dominant controlling mechanism for H-El21A alloy is dislocation climb during creep deformation. Its superior creep resistance was mainly attributed to the pronounced and dense dendritic structure of Mg_3RE intermetallic in the α-Mg hindering the grain boundary sliding and dislocation movement. In addition, the relative homogeneous dispersion of Al_2Zr phase and Al_2Nd phase with a high melting point can also act as efficient reinforcements to inhibit the dislocation movement and benefit the creep properties.

Key words: Magnesium, Elektron21, Creep, high shearing, Aluminium

1. Introduction

Owing to the light weight, good castability and high specific strength, magnesium (Mg) alloys are becoming the focus of interest in many application fields, such as aircrafts, automobiles and commercial electrical products [1-3]. They are beneficial especially for conserving energy, reducing weight and increasing fuel efficiency in the engineering applications [4]. In addition to their remarkable structural properties, Mg alloys also have a good electromagnetic shielding property with those additions of Y, Ce and/or Cu [5-7]. However, creep resistance, as an important criterion to evaluate the dimensional stability at elevated temperatures, is relatively poor for Mg alloys, which limits their wider applications in powertrain applications in a temperature regime above 150 °C [8].

Alloying was often regarded as a promising way to improve the creep resistance of Mg alloys, but its influences are diverse and uncertain. For example, with the addition of Al element in Mg alloys, such as the most commonly used alloy AZ91 (Mg-9Al-1Zn) and AM60 (Mg-6Al-0.3Mn), they often exhibit inferior creep resistance due to the occurrence of low thermal stability phase $Mg_{17}Al_{12}$ in Mg matrix [9, 10]. The additions of rare earth (RE) elements, such as Nd, Gd and Y, were widely reported as an effective way to improve the creep resistance of Mg alloys. Zhu et al. [11] reported that Mg-Nd alloy exhibited better creep resistance compared with Mg-La and Mg-Ce binary alloys due to the supersaturation of Nd elelement in the α-Mg matrix. Suzuki et al. [12] found that the creep properties of Mg were significantly enhanced with the addition of Y as compared with Al and Mn, which was mainly due to the forest dislocation-hardening and dynamic precipitation during creep. Besides, the combination of Al and RE addition in Mg alloys, including AE41 (Mg-4Al-1RE) [13], AE42 (Mg-4Al-2RE) [14], and AE44 (Mg-4Al-4RE) [15], always shows a superior improvement of creep resistance due to the reduction of $Mg_{17}Al_{12}$ phase fraction and the occurrence of Al-RE phase with a high thermal stability. These Mg-Al-RE alloys are usually Zr-free alloys because Al is commonly regarded as the poisoning element for Zr, which interferes grain refinement owing to the formation Al-Zr compound. Nevertheless, Kabirian et al. [16] reported that with the addition of Zr in the range of 0.2-1.0 wt.% in AZ91, its creep resistance was improved apparently due to the formation of Al_2Zr and Al_3Zr_2 intermetallics, which can act as thermal stable barriers to oppose the recovery process. This report implies that the coexistence of Al and Zr in Mg-based alloy might also have positive effect to enhance the creep properties. Katsarou et al. [17] reported that by adding the mixture of Al and ceramic AlN nanoparticles in Zr-containing Mg-RE alloy (Elektron21, Mg-2.8Nd-1.2Gd-0.4Zr-0.3Zn, wt. %), its creep resistance was

significantly improved. Further report from Daudin et al. [18] only researched on the key mechanisms from AlN nanoparticles in improving the creep properties of Elektron21 (El21), but the influences from Al was not yet totally unraveled. Indeed the true detailed effects from Al element on the creep resistance, microstructural modification, and strengthening mechanisms of El21 alloy still requires further investigations.

The solidification process and microstructures of the Mg alloys are also influenced by the stirring treatment prior to solidification. Zhao et al. [19] found that with the ultrasonic treatment, the grain size of Mg–3% Al–1% Zn–0.8% Ce–0.3% Mn alloy was decreased from 136.3 to 44.7 μm compared with non-ultrasonic treated alloy. Its intermetallic MgAlCeMn was also modified from needle-like to a more globular shape. Recently, a high shearing dispersion technique (HSDT), which was invented by BCAST in Brunel university, was applied to stir the melt before solidification [20]. Zhu et al. [21] reported that the high shearing rate introduced by HSDT can lead to a significant grain refinement for AZ91D alloy.

In the present paper, the influence of HSDT before solidification on the microstructural evolutions was investigated. HSDT was used to prepared El21+0.25 wt.% Al alloy. For comparison, non-high sheared El21, non-high sheared 0.25% Al-containing El21 alloy and high-sheared El21 alloy were also produced, respectively. Their creep resistances and microstructures were examined. The responsible mechanisms were discussed.

2. Experimental material and procedures

Commercial magnesium alloy El21 with a composition of Mg-2.85Nd-0.92Gd-0.41Zr-0.29Zn (all compositions are in wt.% unless specified), provided by Magnesium Elektron Ltd at Manchester, UK, was selected as a master alloy. El21 ingots with a weight of 12 kg were molten at 720 °C in a mild steel crucible under a mixed protective gas (Ar+1 vol. % SF_6). 0.25% pure Al was added in the melt at 720 °C and then the melt was subjected to intensive shearing by a Φ 67.5 mm rotor-stator mixer at a speed of 3000 rpm for 1 min. Detailed illustration of the high shearing dispersion technique (HSDT) and its principle can be found elsewhere [22-25]. After high shearing, the melt with a weight of about 3 kg was poured into a cylindrical mould that was preheated to 450 °C and held in a three-zone resistance ring furnace at a constant temperature of 670 °C for 5 min. Then the crucible with the melt was lowered into a water bath at a rate of 100 mm/ min. Similarly, high-sheared El21 (H-El21) base alloy was also prepared using the above process. For comparison, non-high sheared El21 (NH-El21) and non-high sheared El21+0.25% Al alloy (NH-El21A) were also fabricated. Detailed casting

parameters based on the above procedures are listed in **Table** 1. The solidification behaviour of investigated alloys was predicted by Pandat software with the thermodynamic database PanMg 2017. The thermodynamic calculations were performed based on Scheil´s model [22].

Table 1. Casting parameters, grain size and hardness of NH-El21, H-El21, NH-El21A and HS-El21A alloy.

Materials	Composition	High-shearing speed/ rpm	High-shearing time/ min	Grain size/ μm	Hardness/ HV5
NH-El21	El21	-	-	80.1±5.0	45.0±1.2
H-El21	El21	3000	1	59.4±1.7	43.7±1.8
NH-El21A	El21+0.25% Al	-	-	151.3±4.0	50.8±2.5
H-El21A	El21+0.25% Al	3000	1	167.0±5.7	48.2±2.0

Compression creep samples with 15 mm gauge length, 6 mm in diameter were tested at 240 °C and a load from 80 to 140 MPa. Creep tests were performed at Applied Test Systems (ATS) lever arm creep test systems. Two thermocouples with an accuracy of ±1 °C were used to measure the working temperature. The creep strain of the specimens was recorded by an extensometer connecting with the measuring unit. The creep tests were stopped once the minimum creep rate was achieved.

The specimens for optical microscopy (OM) were ground with silicon carbide emery paper up to 2500 grit and then polished using a diamond suspension (1 μm) and colloidal silica (OPS, 0.05 μm). The polished surface was etched in a solution of 8 g picric acid, 5 ml acetic acid, 10 ml distilled water and 100 ml ethanol. Optical microstructures were characterized using a Leica DMI5000 with a digital camera. The average grain size was measured by the linear intercept method [26]. Microstructural observations were performed by a scanning electron microscope (SEM) equipped with Tescan energy dispersive X-ray (EDX) spectrometer (TESCAN VEGA3-SB, Brno, Czech Republic). Phase analyses were performed on the high-energy X-ray beamline HEMS P07B at PETRA III (DESY, Hamburg) with a wave length λ=0.01424 nm. The thin foils for further transmission electron microscopy (TEM) characterization were prepared by a 30 keV Gaþ focused ion beam (FIB) in a Nova-200 dual-beam SEM. TEM examinations were characterized by a Philips CM 200 (FEI Company, Netherlands) equipped with an EDS system operating at 200 kV.

3. Results

3.1 Creep properties

The typical creep rate curves of four alloys tested at 240 °C under various applied stresses from 80-140 MPa are shown in **Fig**. **1**. The creep rates were calculated by taking the time derivative from creep strain. It can be seen that the creep rates reduce rapidly during the primary creep stage and then experience a steady-state region for all alloys. The minimum creep rates of NH-El21 and H-El21 alloys are much higher than that of NH-El21A and H-El21A alloys under all applied stresses, demonstrating that the addition of 0.25% Al can enhance the creep resistances of El21 alloy. The creep curves of NH-El21 and H-El21 alloys are very close, implying that only fabricating with HSDT has no obvious positive effects on the creep properties of El21. However, the creep rates of H-El21A are obviously lower than that of NH-El21A under the loads from 80-140 MPa. It exhibits a superior creep resistance by about more than half an order of magnitude than that of NH-El21A alloy without HSDT (**Table 2**). This indicates that HSDT can enhance the creep resistance only when Al was added in El21 alloy. Among these four alloys, H-El21A alloy has the best creep resistance under the stress from 80-140 MPa (**Fig. 1**). With the assistance of HSDT, the minimum creep rate of H-El21A under 140 MPa (2.68×10^{-7} s^{-1}) exhibits about one order of magnitude lower than that of NH-El21 alloy (3.68×10^{-6} s^{-1}) and H-El21 alloy (4.01×10^{-6} s^{-1}) (**Table 2**).

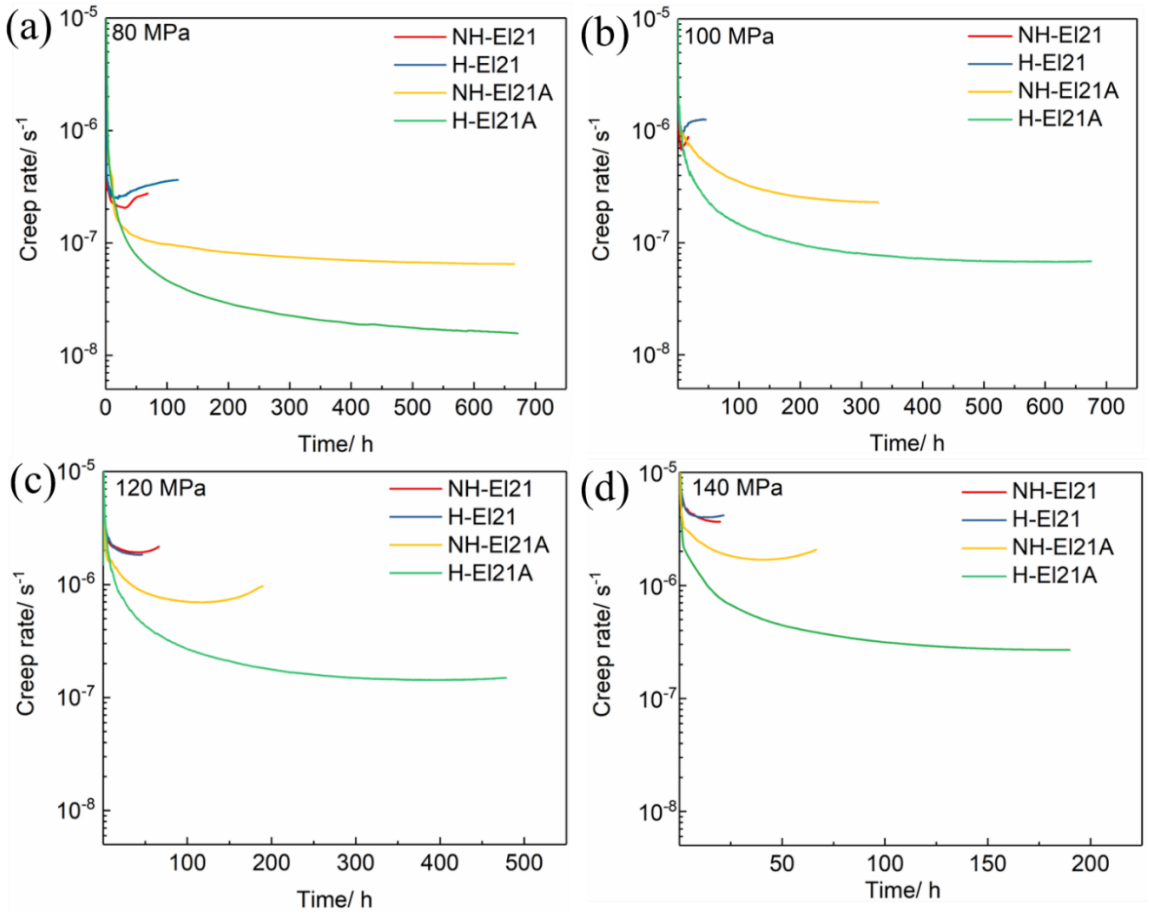

Fig. 1. Creep rate over time for NH-El21, H-El21, NH-El21A and H-El21A at 240 °C and under applied stresses of (a) 80 MPa, (b) 100 MPa, (c) 120 MPa and (d) 140 MPa.

Table 2. Minimum creep rates at different applied stresses.

Materials	Stress/ MPa	$\dot{\varepsilon}$/ s^{-1}
NH-El21	80	2.06×10^{-7}
	100	6.87×10^{-7}
	120	1.88×10^{-6}
	140	3.68×10^{-6}
H-El21	80	2.5×10^{-7}
	100	9.25×10^{-7}
	120	1.83×10^{-6}
	140	4.01×10^{-6}
NH-El21A	80	6.57×10^{-8}
	100	2.31×10^{-7}
	120	6.95×10^{-7}
	140	1.68×10^{-6}
H-El21A	80	1.56×10^{-8}
	100	6.71×10^{-8}
	120	1.47×10^{-7}
	140	2.68×10^{-7}

3.2 Microstructural characterizations

Fig. 2 shows the optical microstructures of NH-El21, H-El21, NH-El21A and H-El21A alloys, respectively. The grain sizes and hardness of four alloys are listed in **Table 1**. NH-El21 alloy shows equiaxed grains with an average grain size of 80.1±5.0 μm (**Fig. 2**(a)). With the assistance of HSDT, the grain size decreases to an average size of 59.4±1.7 μm (**Fig. 2(b)**). After adding 0.25% Al to El21 alloy, the morphology of grains was transformed from equiaxed to typical dendritic grains (**Fig. 2** (c-d)). Compared with NH-El21 and H-El21 alloys, these Al-containing El21 alloys exhibit coarsening grains in **Fig. 2**(c-d) (151.3±4.0 and 167.0±5.7 μm). Moreover, with the assistance of HSDT, the dendrite arms in H-El21A are more pronounced in the α-Mg regions than that in NH-El21A alloy (red arrows in **Fig. 2**(c-d)). This phenomenon reveals that the addition of 0.25% Al could influence the morphology of grains and the growth process of dendritic arms.

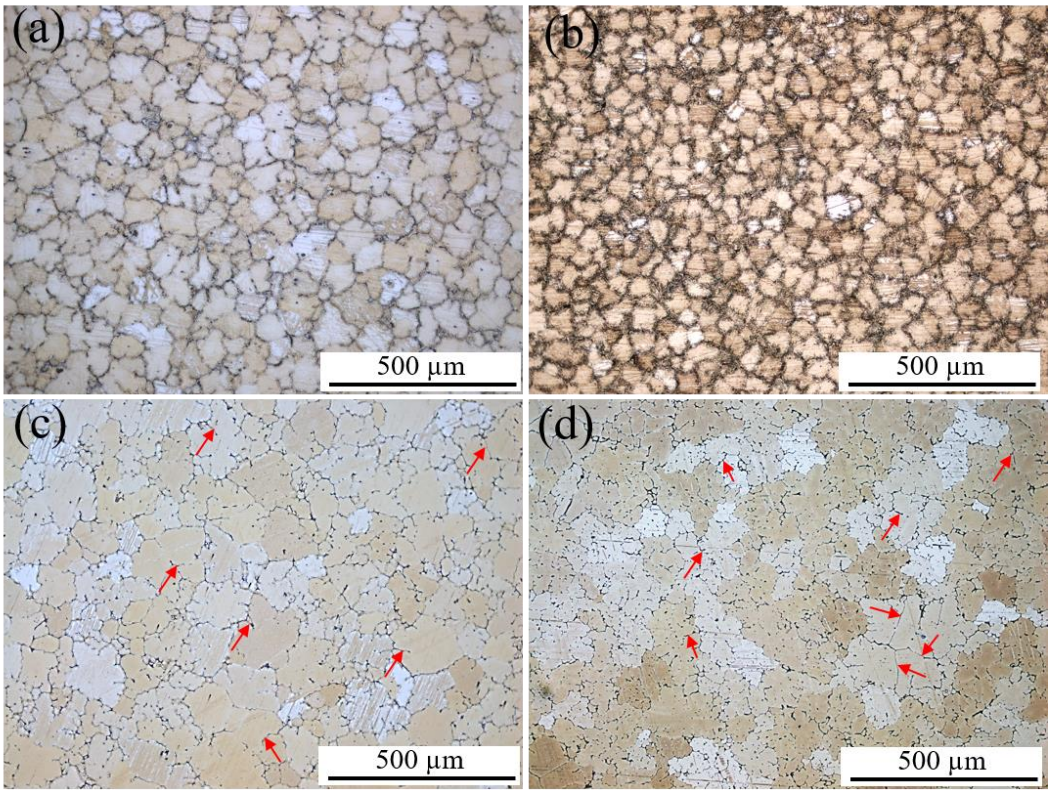

Fig. 2. Optical microstructures of as cast (a) NH-El21, (b) H-El21, (c) NH-El21A and (d) H-El21A alloys.

The high-energy X-ray diffraction (XRD) patterns were shown in **Fig. 3**. In addition to the typical α-Mg peaks, the peaks corresponding to Mg_3RE phase is also observed (**Fig. 3**(a)), indicating Mg_3RE phase is the dominant intermetallic phase in El21 alloy. There are also a few very low peaks between 2-3 °, which might be identified as Mg_5Gd phases. With the addition of 0.25% Al, no additional peak was detected (**Fig. 3**(b)). However, it cannot be excluded that some additional phases were possibly formed after the addition of 0.25% Al. Due to the slight content of Al, it may still be difficult for high-energy XRD to detect such very small amount of phases. The morphologies of intermetallics were observed using BSE imaging technique (**Fig. 4**). NH-El21 and H-El21 alloys exhibit similar morphologies of network intermetallics with primary α-Mg and white eutectic Mg_3RE (**Fig. 4** (a) and (b)). Due to the very low intensity of the peaks in **Fig. 3** for Mg_5Gd phases, they may combined together with Mg_3RE and make it hard to identify them separately. Herein the intermetallics are all considered as Mg_3RE phases. With the addition of 0.25% Al, the morphology of intermetallics was changed to a continuous network with apparent dendritic arms (**Fig. 4** (c)). In particular, the H-El21A alloy with high shearing shows more pronounced dendritic arms than NH-El21A alloy (**Fig. 4** (d)). The distribution of intermetallics in H-El21A alloy is obviously denser than that in NH-El21A alloy.

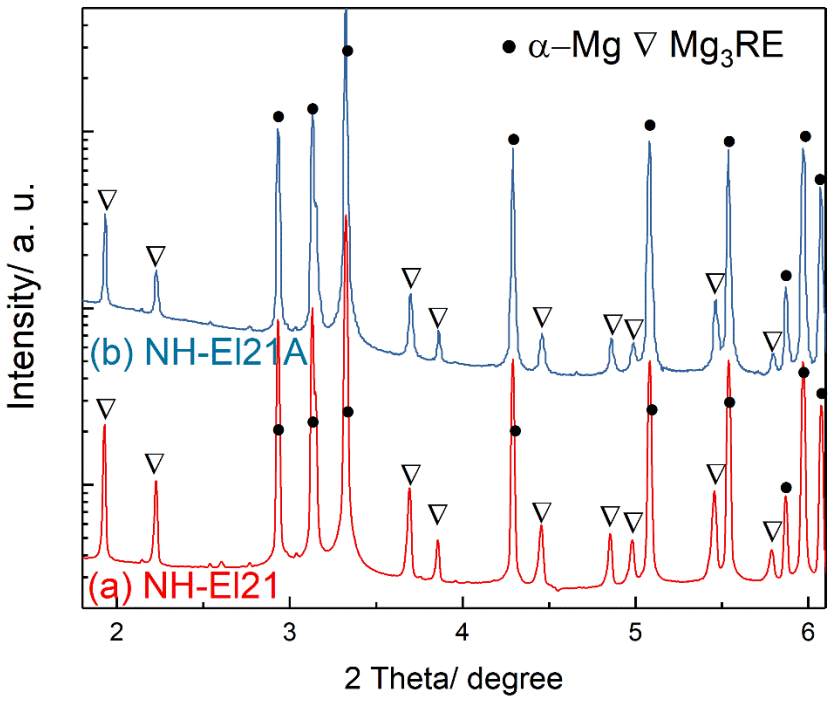

Fig. 3. High-energy XRD patterns of the as cast (a) NH-El21 and (b) NH-El21A.

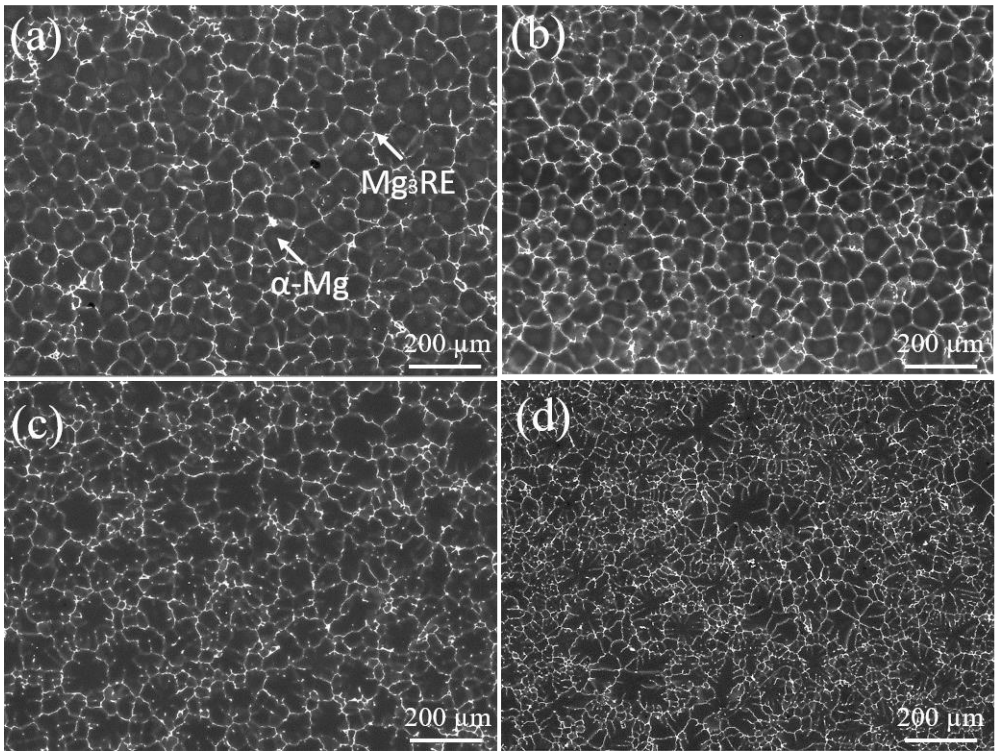

Fig. 4. Back scattered electron (BSE) SEM images of as cast (a) NH-El21, (b) H-El21, (c) NH-El21A and (d) H-El21A alloys.

Besides the eutectic phase, many lath-like precipitates were observed near the eutectic in NH-El21 and H-El21 alloys (green arrows in **Fig. 5**(a) and (b)). Due to the slight content of these precipitates, it is difficult to identify them by high-energy XRD. Liu et al. [27] confirmed these lath-like precipitates were $Mg_{12}Nd$ with a tetragonal structure using TEM. These $Mg_{12}Nd$ precipitates are commonly formed in Mg-Nd based alloys, which is associated with the supersaturated solid solution of Nd element [28, 29]. However, such precipitates can hardly be detected in NH-El21A and H-El21A alloy (**Fig. 5**(c-d)). This demonstrates that the formation of $Mg_{12}Nd$ precipitates was suppressed by adding Al in combination with HSDT. The existence of Al element and HSDT played an important role in influencing the formation of second phases.

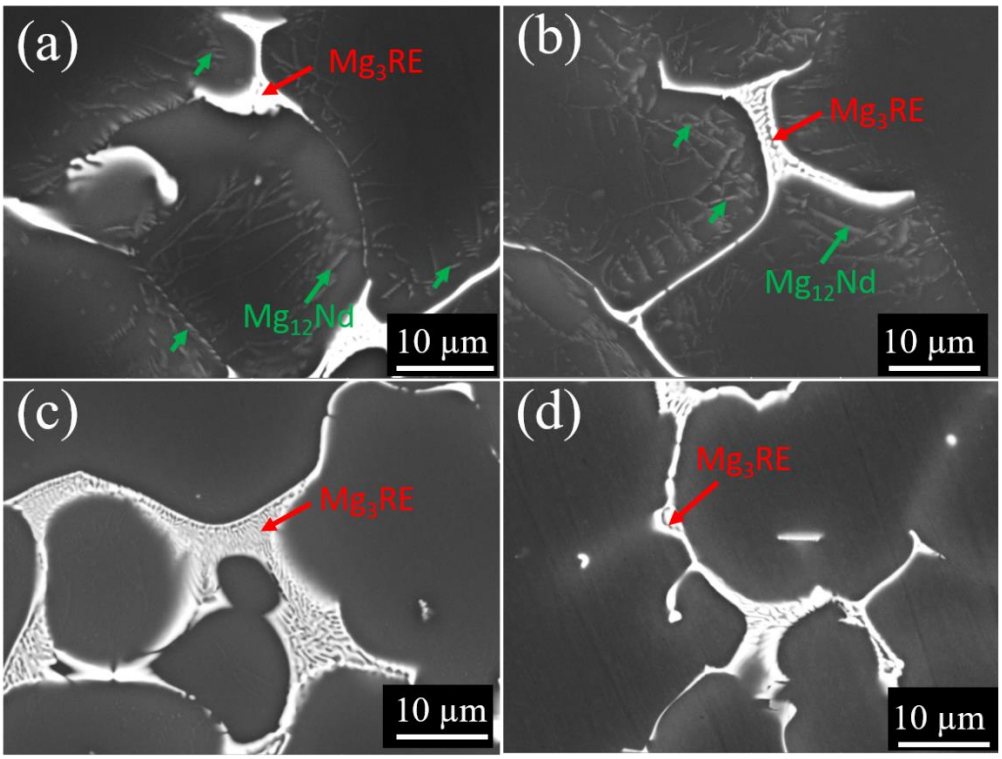

Fig. 5. BSE images of as cast (a) NH-El21, (b) H-El21, (c) NH-El21A and (d) H-El21A alloys.

3.3 Phase identifications

The bright dotted particles located in the centre of α-Mg grains were identified to be α(Zr) phase, which shows a high concentration of Zr using EDS analysis (**Fig. 6**). With the addition of 0.25% Al in El21 alloy, besides those network intermetallics, many bright block-shaped particles were observed in NH-El21A alloy Fig**. 7**(a)). They agglomerated as clusters in the matrix. Some of these block-shaped particles are located inside the α-Mg grains (green arrow). Some of them were pushed to the solid-liquid interface during solidification and connected with eutectic phases (yellow arrow). The corresponding EDS result of the block-shaped particle (red cross position in (b)) reveals that it is mainly comprised of Al and Zr elements (**Fig. 7**(c)). It is widely reported that Al is prone to react with Zr to form the stable intermediate phase such as Al_3Zr [30, 31], Al_2Zr_3 [32-34] and Al_2Zr [35, 36]. Based on the statistical analyses of 20 EDS quantitative points, the average ratio of Zr to Al was obtained as 1.22±0.03, which is close to the Al_2Zr_3 phase ratio (Zr/Al=1.5). Tamim [37] proposed that Al_2Zr_3 phase has a tetragonal crystal structure.

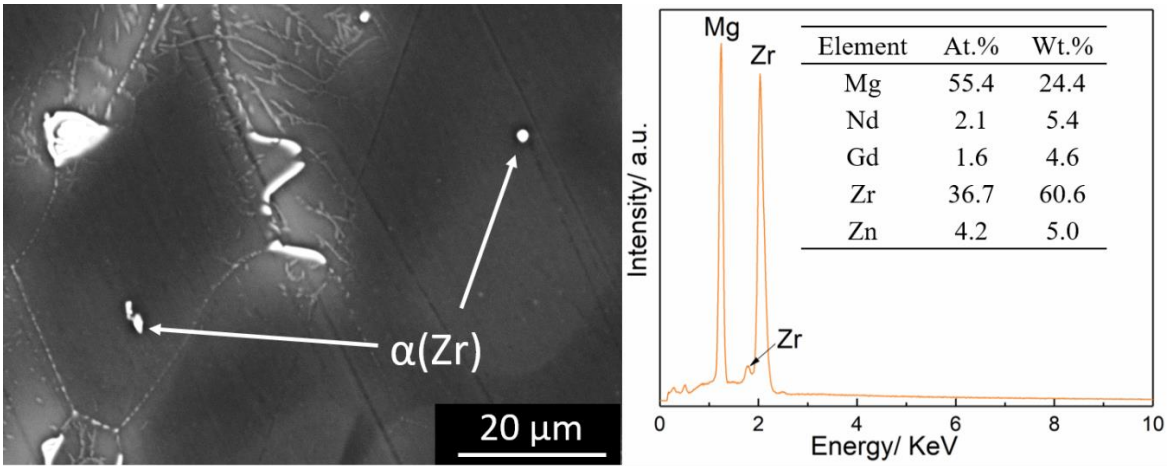

Element	At.%	Wt.%
Mg	55.4	24.4
Nd	2.1	5.4
Gd	1.6	4.6
Zr	36.7	60.6
Zn	4.2	5.0

Fig. 6. BSE images and the corresponding EDS result of as cast NH-El21 alloy.

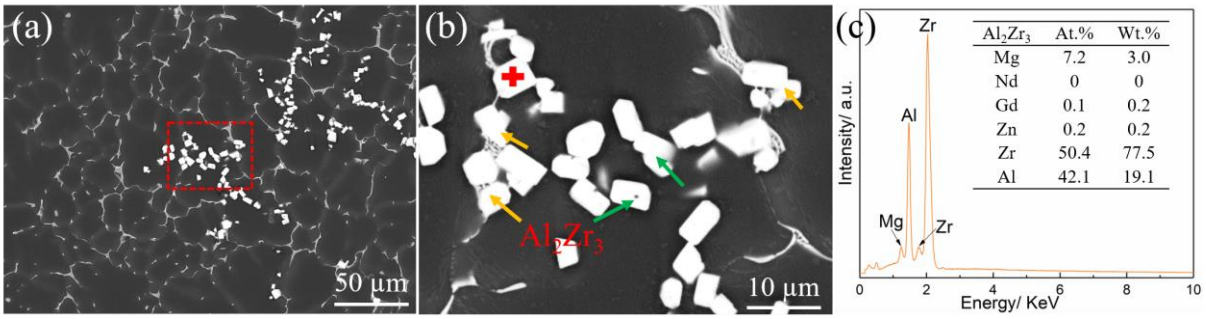

Al_2Zr_3	At.%	Wt.%
Mg	7.2	3.0
Nd	0	0
Gd	0.1	0.2
Zn	0.2	0.2
Zr	50.4	77.5
Al	42.1	19.1

Fig. 7. BSE images of as cast (a) NH-El21A alloy, (b) magnified image for the rectangular position in (a) and (c) the corresponding EDS result for the position in (b).

The microstructures of H-El21A are shown in **Fig. 8**. Unlike the Al_2Zr_3 phase in H-El21A, the agglomerations of bright particles was relatively decreased inside H-El21A alloy after HSDT, which were observed separately inside the grains (**Fig. 8**(a)). The shape of these bright particles (particulates) are different from that of those particles (block) in NH-El21A alloy (**Fig. 7**(b) and **Fig. 8**(b)). EDS analyses in **Fig. 8**(c) indicates that this particulate phase is mainly made up of Al and Zr (A area in **Fig. 8**(b)). This similar morphology of Al-Zr phase was also characterized by Lakshman et al. [38] using SEM. In **Fig. 8**(c), the atomic content of Al is higher than that of Zr. Quantitative calculations with 20 EDS points unraveled the average ratio of Zr to Al is 0.56±0.02. Hence, the particle at point A was identified as Al_2Zr phase (Zr/Al=0.5). Next to the particle A, the particles B and C with dark grey and light grey were also identified, respectively (**Fig. 8**(b)). The corresponding EDS analyses exhibited that both particles B and C have high concentrations of Al and Zr. The only difference is that particle B is an Al-rich phase and particle C is a Zr-rich phase (**Fig. 8**(d) and (e)). In addition, the EDS line-scan analysis also shows that particle C has a much higher Zr concentration than particle

B. With the quantitative calculations of EDS analysis, the Zr/Al ratios for particles B and C are 0.58 and 1.23, respectively. Consequently, the particles B and C are identified as Al_2Zr and Al_2Zr_3 phases, respectively. Noting that the amount of this shell structure phase (Al_2Zr+Al_2Zr_3 at B and C) is much smaller than that of Al_2Zr phase in H-El21A alloy.

Hence, it is reasonable to conclude that without the addition of 0.25% Al, Zr acted as an isolated nucleation core in El21 alloy (**Fig. 6**). When 0.25% Al was added into El21, Zr easily reacted with it to form different Al-Zr intermediate phases. In NH-El21A alloy Al_2Zr_3 phase was found to be the dominant Al-Zr phase. In H-El21A alloy with high shearing, Al_2Zr phase is the main Al-Zr phase. Besides, a few shell structure phases (Al_2Zr+Al_2Zr_3) were also detected. In summary, both the addition of Al element and the employment of HSDT chemically influence the formation of Al-Zr compound during solidification.

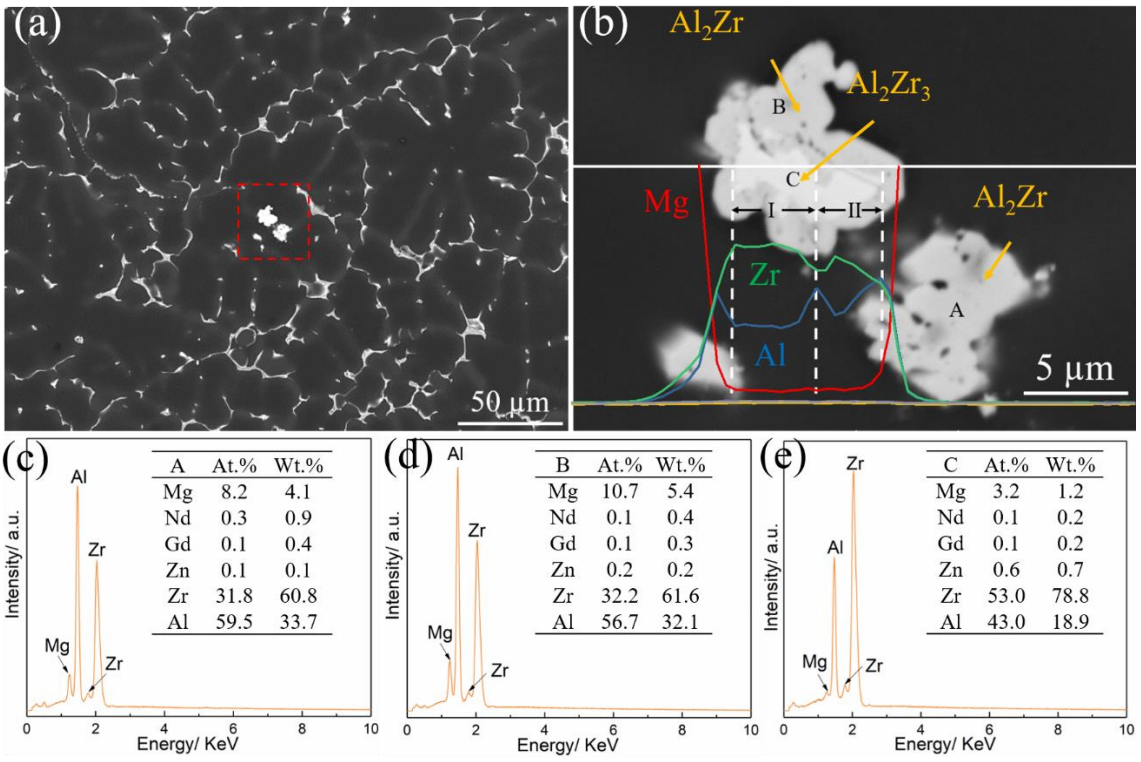

Fig. 8. (a) BSE images of as cast H-El21A alloy, (b) magnified image of the rectangular position in (a) and (c)-(e) are EDS analyses corresponding to A, B, C areas in (b).

In addition to aforementioned Mg_3RE and Al-Zr intermetallics, a small amount of additional Al-RE phases at three different formation positions were also observed in H-El21A alloy, respectively (**Fig. 9**). First, Al-RE particle at P1 was entrapped by the eutectic Mg_3RE (**Fig.**

9(a)). Second, Al-RE particle at P2 is a separated core in the α-Mg matrix (**Fig. 9**(b)). Third, Al-RE particles at P3 and P4 are connected with the intermetallic Mg_3RE (Fig. 9(c)). **Fig. 10**(a) shows the TEM micrographs of the intermetallics in H-El21A alloy. Particle A is mainly composed of Mg and RE element, which is already confirmed as Mg_3RE phase according to high-energy XRD patterns (**Fig. 10**(b)). Particle B is connected closely with Mg_3RE phase which contains high amounts of Al (39.8 at. %) as well as RE element (20.7 at.% Nd and 7.7 at.% Gd) (**Fig. 10**(c)). This Al-RE particle is fairly small (about 100 nm) that made it difficult to obtain the corresponding electron diffraction patterns. Previous researchers [39, 40] reported that Al_2RE (face-centred cubic structure) and $Al_{11}RE_3$ (body-centred orthorhombic structure) phases are two dominant phases in Mg-Al-RE alloys, such as AE42 [41] and AE44 [15] alloys. The chemical formula of Al-RE phase is found to have a close relationship with the content of RE. Zhang et al. [42] claimed that the preferentially formed Al-Nd phase is Al_2Nd when the content of Nd is below 4%. Further addition of Nd to 6% leads to the occurrence of $Al_{11}Nd_3$ phase in Mg-4Al-based alloy. In addition, they [42] reported that the morphologies of the Al_2Nd and $Al_{11}Nd_3$ phases are distinctly different. $Al_{11}Nd_3$ phase usually exhibits lamellar-like morphology and Al_2Nd phase is particulate. Their result is also in agreement with that reported by other literatures [15, 41, 43]. In the present result, the content of Nd in El21 is 2.85%, which is lower than 4%. It implies that Al_2Nd phase might be formed instead of $Al_{11}Nd_3$ phase in H-El21A alloy. According to the corresponding EDS result (**Fig. 10**(c)), the ratio of Al to Nd is about 1.92, which is almost identical to the atomic ratio of Al_2Nd. Therefore, it can be concluded that the particle B is Al_2Nd phase (**Fig. 10**(a)). Saboori et al. [44] also detected the Al_2Nd phase using XRD, which was caused by the reaction of Nd with Al in 2% AlN/Al nanoparticles reinforced El21 composites. Their result further validates the formation of Al_2Nd phase in the present investigation.

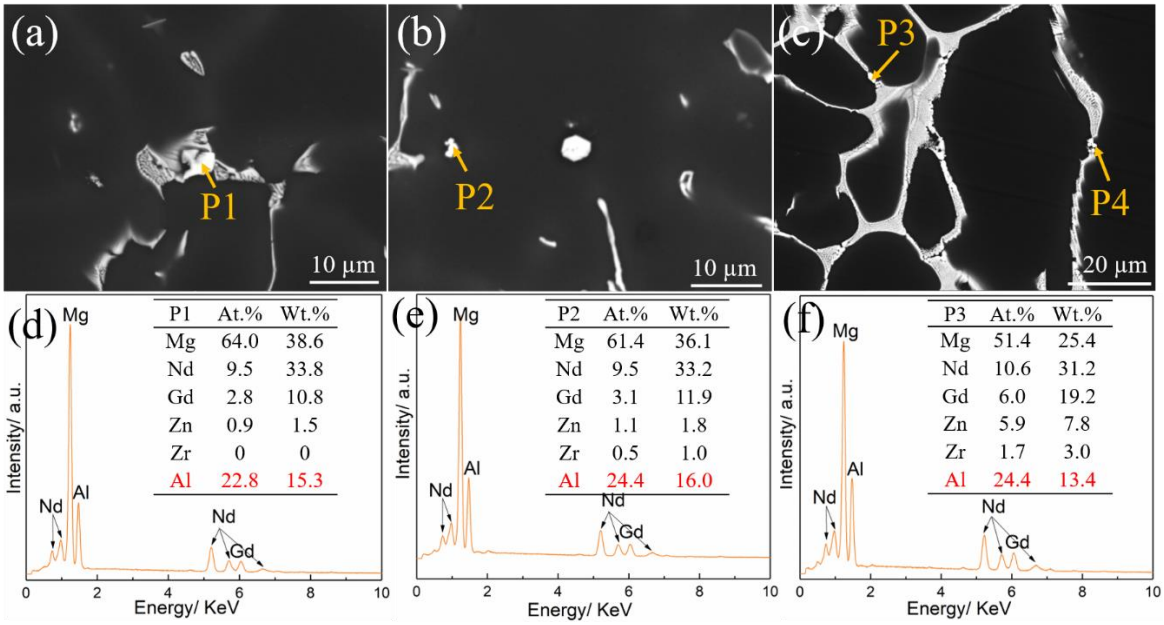

Fig. 9. (a), (b) and (c) BSE images of as cast H-El21A alloy, d), (e) and (f) the EDS analyses corresponding to (a), (b) and (c), respectively.

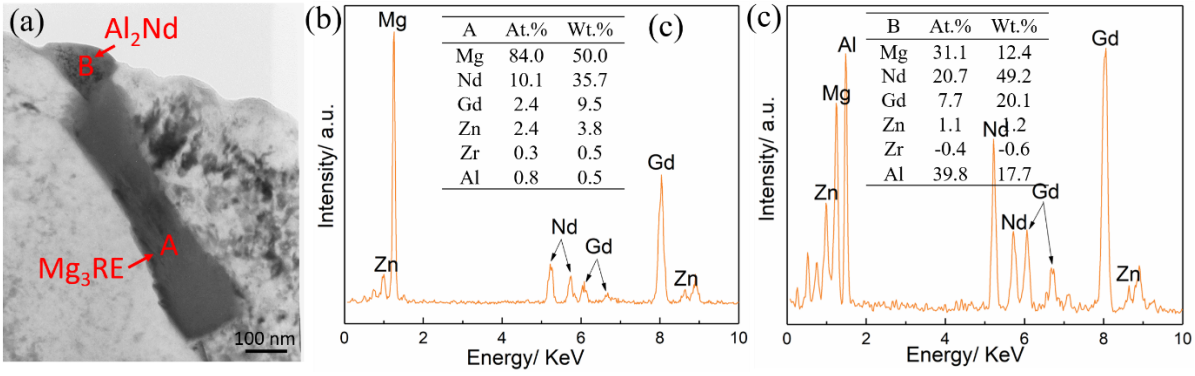

Fig. 10. (a) TEM micrograph of the phase in the as cast H-El21A alloy, (b-c) the corresponding EDS analyses of particles A and B.

4. Discussion

4.1 Microstructure

4.1.1 Grain size and morphology

Fig. 11 shows the average grain size for NH-El21, H-El21, NH-El21A and H-El21A alloys. With the assistance of HSDT, the grain size of H-El21 alloy obviously reduces compared with NH-El21 alloy. The reason for such an obvious grain refinement is owing to the refining efficiency of MgO particles generating from intensive shearing [23]. It was reported that MgO can act as potential nucleation sites for α-Mg during solidification. Fan et al. [24] observed the average grain size of AZ91D alloy was reduced from 682 to 187 μm after the employment of

HSDT. After adding 0.25% Al in El21 alloy (NH-El21A and H-El21A), the grains coarsen. This is attributed to the poison effect resulting from Al in Zr-containing El21 alloy. Normally, Zr element, which was observed as an isolated core in non-Al containing El21 alloy (**Fig. 6**), is regarded as an effective nucleant site for α-Mg during solidification [45]. The present addition of 0.25% Al in El21 alloy results in the formation of Al_2Zr_3 and Al_2Zr phases in NH-El21A and H-El21A alloys (**Fig. 7** and **Fig. 8**), respectively. The interaction of Al with Zr consumed a certain amount of Zr and consequently deteriorated the grain refinement effect of Zr for El21 alloy.

The use of HSDT also influences the grain size. After HSDT, the grain size of H-El21A alloy (167.0±5.7 μm) increases compared with NH-El21A alloy (151.3±4.0 μm). HSDT with special rotor-stator design can create an intense friction and high shear stress in the melt, which is beneficial for stirring the melt homogeneously prior to solidification. This effective shearing promoted the possibilities of contacts between Al and Zr. As a result, the reaction of Al with Zr to form Al-Zr compound was enhanced during solidification. The grain coarsening occurred in H-El21A alloy is due to more consumption of grain refiner Zr, although the use of HSDT is beneficial for the grain refinement of the same alloy.

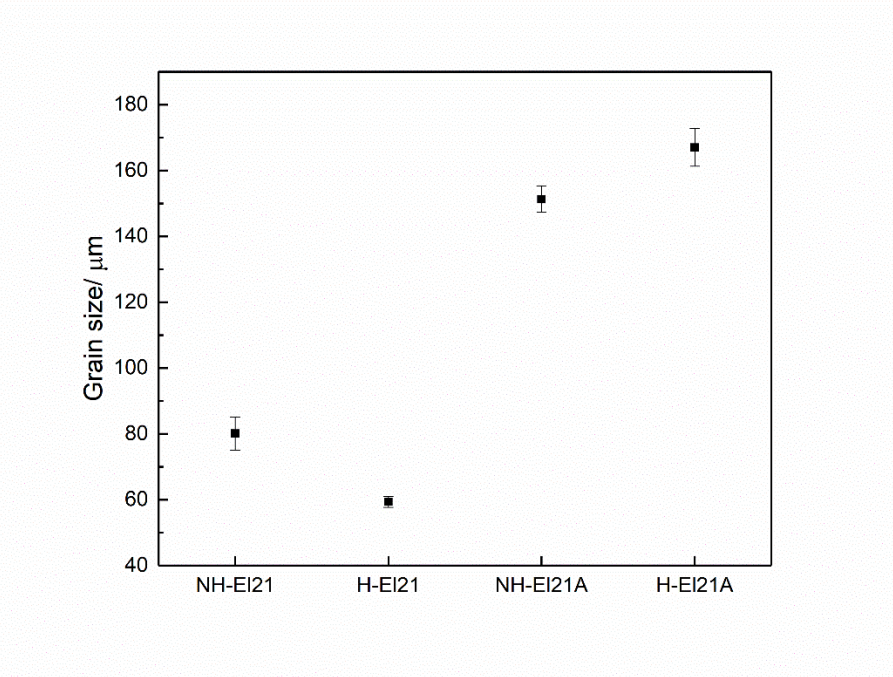

Fig. 11. Average grain sizes for the as cast NH-El21, H-El21, NH-El21A and H-El21A alloys.

Besides the differences in grain size, the grain morphology was also changed from equiaxed to dendritic with the addition of 0.25% Al (**Fig. 2**). This morphology transformation might

derive from the solute segregation power of Al. Recent research stated that solute segregation power can be quantified using growth restriction factor (GRF), or *Q*-value [46]. In a binary system, the GRF value can be simply defined as: $Q= mC_0 (k-1)$ [47] (C_0 is concentration of solute, *m* is the slope of the liquidus, *k* is the solute distribution coefficient). The higher *Q* values signified the higher tendency of the solute to introduce constitutional supercooling aheaed of the advancing solid/liquid interface. It is reported that Al has a strong segregation power (*Q*=5.31 [48]) in Mg alloys and results in a significant constitutional supercooling ahead of solid/liquid interface, thus making α-Mg grow easily by dendritic type. This result is in agreement with Jiang's report [48]. They also observed a typical dendritic growth in the Al-modified Mg-5Sn-0.3Li alloy. Moreover, with the employment of HSDT in H-El21A alloy, the outline of dendritic arms are more pronounced (**Fig. 2**(c-d)). The dendritic arm spacing (DAS) was calculated as: DAS=*L/n*, where *L* is the distance of the line drawn from edge to edge of the measured grains, *n* is the number of the dendritic cells [49]. The DAS of H-El21A is 56.2±1.6 μm, which is finer than that of NH-El21A alloy with a DAS of 74.0±6.4 μm. It indicates that the DAS largely decreases using HSDT in Al-containing El21 alloy. The reason can be ascribed to the more homogeneous dispersion of Al atoms in the melt using HSDT prior to solidification, which can play a more effective role in creating a constitutional supercooling ahead of the solid/liquid interface during solidification, and therefore reduce the DAS.

4.1.2 Phase formation

The intermetallic morphologies of NH-El21 and H-El21 alloys were modified from continuous network to branched dendrite after the addition of 0.25% Al (**Fig. 4**). In addition, there is almost no intermetallics formed inside α-Mg grains for NH-El21and H-El21 alloys (**Fig. 4**(a-b)). In contrast, many dendritic arms were formed in the interdendritic regions, especially in H-El21A with compact hyper-branched intermetallics (**Fig. 2** (d)). Thermodynamic calculation for El21 using Pandat software shows that the primary α-Mg solidifies over a wide range of 117 °C (528-645 °C), whereas the solidification of Mg_3RE intermetallics occurs only in the last 6 °C (528-534 °C) (**Fig. 12**(a)). This indicates that Mg_3RE intermetallics solidified at the latest stage among the dendrite arms after most α-Mg grains were formed. The morphology of the intermetallics is thus a footprint of the solidification of these branched dendrites. Since the grains changed from equiaxed to dendrite with the addition of 0.25% Al, the morphology of Mg_3RE intermetallics is therefore modified to branched dendrite morphologies.

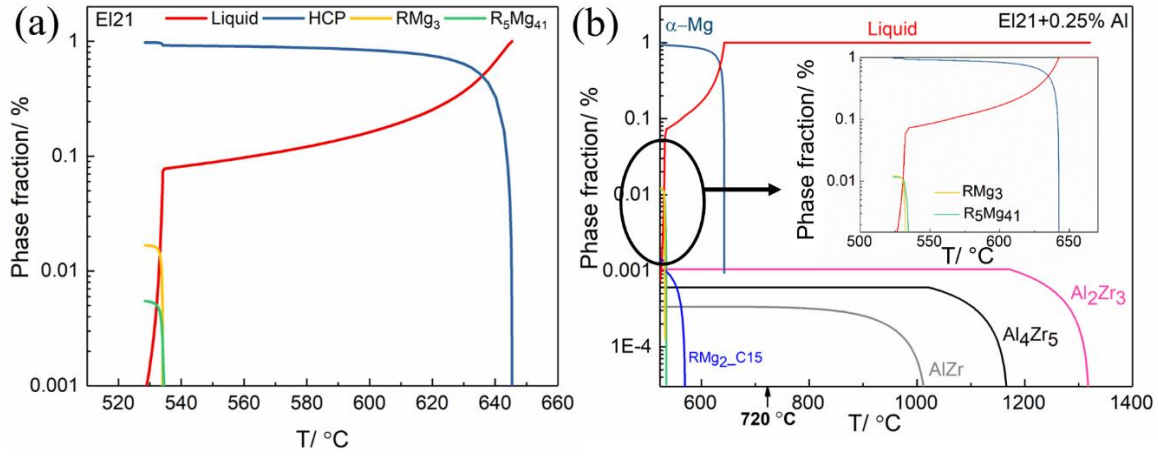

Fig. 12. Mass fraction of the phases calculated under Scheil´s condition (a) El21 and (b) El21+0.25% Al. The region marked with a black circle was magnified to that at the top right corner, which indicates the phase fraction evolution of RMg_3 and $R5Mg_{41}$ during solidification (R indicates RE here).

The $Mg_{12}Nd$ precipitates, which were originally formed near eutectic phases in NH-El21 and H-El21 alloys, become difficult to be observed in Al-containing El21 (**Fig. 5**(c-d)). The formation of Al_2Nd phase in H-El21A validated that some RE atoms were captured by Al, which consequently alleviated the supersaturated Nd element in the α-Mg matrix. Therefore, the formation of $Mg_{12}Nd$ precipitates was suppressed in the alloys with the addition of 0.25% Al.

Based on the phase characterizations using SEM in NH-El21A, Al reacted with Zr to form Al_2Zr_3 phase. No obvious Al-RE phases could be observed (**Fig. 7**). These results are consistent with that obtained by the thermodynamic calculations for El21+0.25% Al alloy (**Fig. 12**(b)). With the assistance of HSDT, the Al_2Zr phase becomes the dominant Al-Zr phase in H-El21A alloy instead of Al_2Zr_3 phase (**Fig. 8**). This result is inconsistent with that obtained by thermodynamic calculations (**Fig. 12**(b)). Murray et al. [50] proposed that Al_2Zr_3 phase might occur in Al-Zr alloys with a content of 39 at.% Al. Al_2Zr phase is a Al-rich phase formed with a content of 68.8 at.% Al in Al-Zr alloy. The increment in the content of Al could lead to a composition transformation from Zr-rich phase (Al_2Zr_3) to Al-rich phase (Al_2Zr). As for H-El21A alloy, HSDT could create high shear stress to stir the melt and increase the probabilities of contacts between Al and Zr. This effect facilitates more Al atoms to involve in the Al-Zr reaction. Thus, Al_2Zr phase becomes preferentially to form in H-El21A alloy. In H-El21A alloy, the shell structure with Al_2Zr+Al_2Zr_3 phases was also observed (**Fig. 8**(b)), indicating that

HSDT is still insufficient to promote the phase transformation from Al_2Zr_3 to Al_2Zr phase completely. Only could the outer layer of Al_2Zr_3 be transformed into Al_2Zr phase. The core is still kept with Al_2Zr_3 phase. It is hereby noted that the distribution of the Al-Zr phase was also influenced by HSDT. The Al_2Zr_3 phase in NH-El21A alloy is prone to agglomerate in the matrix (**Fig. 7**). However, in H-El21A with HSDT it is difficult to observe the discernible agglomeration of Al_2Zr phase (**Fig. 8**). This phenomenon strongly suggests that HSDT is also beneficial for breaking up the clusters of intermetallic phases.

In the present investigation, an additional phase Al_2Nd with small amount was detected in H-El21A alloy rather than in NH-El21A alloy. This is inconsistent with the results of thermodynamic calculations for El21+0.25% Al alloy in which no Al-RE phase was predicted (**Fig. 12**(b)). It is therefore worthwhile to consider the influence of HSDT on the solidification process of H-El21A alloy.

In El21 alloy with the addition of 0.25% Al, Mg-Al, Mg-RE (Mg-Nd and Mg-Gd), Al-RE (Al-Nd and Al-Gd) and Al-Zr binary interactions might happen, but their preferential reaction sequence still remains unknown. Miedema et al. [51, 52] proposed a semi-empirical model to calculate the standard molar enthalpies of formation (ΔH) for these binary systems. The lower the standard molar enthalpies of formation the higher the bond energy, the better the thermal stability and the more the energy releases during their chemical reactions. Consequently, the binary systems with lower ΔH react more preferentially at the same condition. The Miedema model to calculate ΔH can be expressed as:

$$\Delta H = f_{ij} \frac{x_i(1+\mu_i x_j(\Phi_i-\Phi_j))x_j(1+\mu_j x_i(\Phi_j-\Phi_i))}{x_i V_i^{2/3}\left(1+\mu_i x_j(\Phi_i-\Phi_j)\right)+x_j V_j^{2/3}(1+\mu_j x_i(\Phi_j-\Phi_i))} \quad (1)$$

Where x_i and x_j are the mole fractions of *i* and *j*, V_i and V_j are the mole volumes of *i* and *j*, Φ_i and Φ_j are the electronegativities of *i* and *j*, respectively, μ is the empirical parameter. f_{ij} can be rewritten as following:

$$f_{ij}=2pV_i^{2/3}V_j^{2/3}\frac{q/p((n_{ws}^{1/3})_j-(n_{ws}^{1/3})_i)^2-(\Phi_i-\Phi_j)^2-\alpha(r/p)}{(n_{ws}^{\frac{1}{3}})_i^{-1}+(n_{ws}^{\frac{1}{3}})_j^{-1}} \quad (2)$$

Where $n^i{}_{ws}$ and $n^j{}_{ws}$are the electron density parameters, respectively, *p*, *q*, *r* and α are the empirical parameters. Based on the data referred from [52], the curves of formation enthalpy as a function of mole fraction are plotted in **Fig. 13**. Al-Zr system exhibits the lowest ΔH among all the binary systems, suggesting that Al-Zr phase prefers to be formed firstly in

El21+0.25% Al alloy. This result is consistent with the observation of Al_2Zr_3 phase in NH-El21A alloy. Al-RE system shows the second lowest value of ΔH, indicating that Al would preferentially react with RE to form Al-RE phase rather than with Mg to form Mg-Al phase. Previous investigations also demonstrated that Al_2RE (Al-Nd and Al-Gd) phase was preferentially formed instead of $Mg_{17}Al_{12}$ in AE42 alloy [53, 54]. It is reasonable to assume that with the employment of HSDT, Al_2RE phase was formed in El21+0.25% Al alloy besides Al-Zr phase. The molten El21+0.25% Al was intensively sheared by HSDT, which increases the likelihood of mutual contacts between each atoms. Consequently, Al and Nd atoms were promoted to involve in the reaction to form Al_2Nd phase.

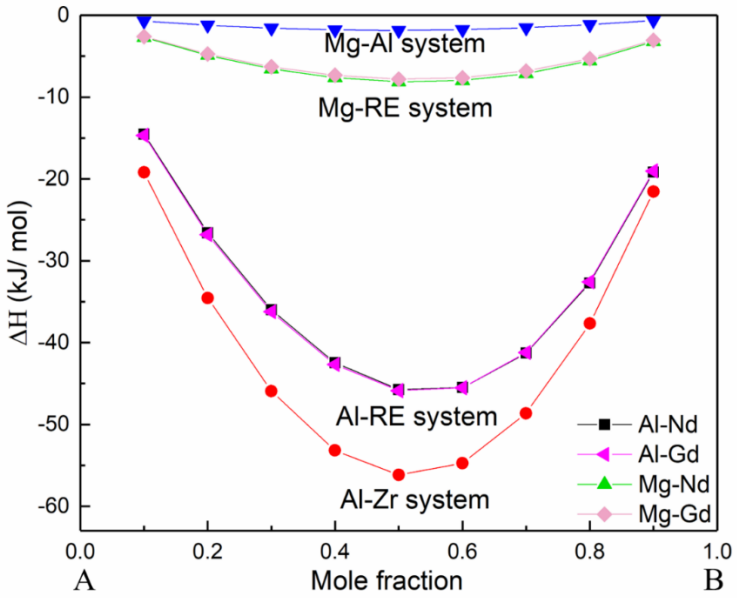

Fig. 13. Formation enthalpies of Mg-Al, Mg-Nd, Mg-Gd, Al-Nd, Al-Gd and Al-Zr binary systems (A-B binary systems).

4.2 Creep mechanisms

4.2.1 Creep data analysis

In order to explain the creep mechanism, the minimum creep rate $\dot{\varepsilon}$ depending on various applied stresses σ is shown in **Fig. 14** (a). The stress exponent n was then calculated by **Eq. (3)** [55]:

$$n = \left(\frac{\partial ln\dot{\varepsilon}}{\partial ln\sigma}\right)_T \quad (3)$$

When the creep temperature T is fixed, the stress exponent n was determined by linear fitting the slopes of the double logarithm of minimum creep rate vs applied stress. The n values for these alloys vary around 5 at 240 °C (**Fig. 14**(a)). As for El21 alloy with large amount of intermetallics, a threshold stress σ_{thr} was necessarily introduced to consider the interaction between dislocations and dispersoid obstacles [56]. **Eq. (4)** describes the relationship between effective stress σ_{eff} and σ_{thr}.

$$\sigma_{eff} = \sigma - \sigma_{thr} \qquad (4)$$

The σ_{thr} was calculated as the lower stress limit below that no creep occurs. Based on Li and Langdon´s model [56], σ_{thr} is calculated by the extrapolation of the double logarithmic curves of $\dot{\varepsilon}$ over σ to a value of 10^{-10} s^{-1}. The σ_{thr} of H-El21A is the highest among these four alloys (28.7 MPa) (**Table 3**), indicating the combination of HSDT with 0.25% Al addition gives a rise in the threshold stress of El21 alloy.

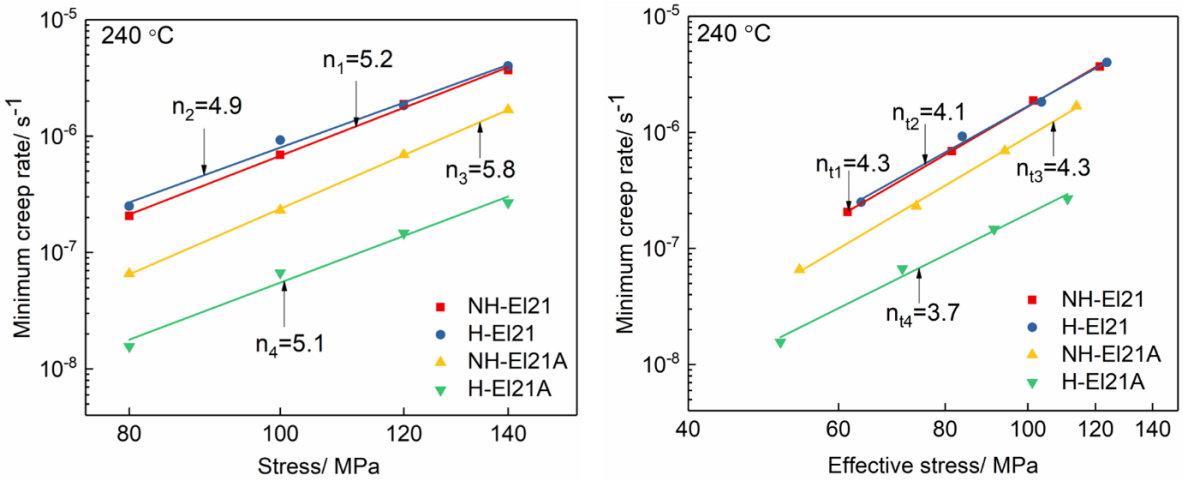

Fig. 14. (a) Stress exponent n, (b) true stress exponents n_t of these four alloys.

Table 3. Values of stress exponent n, threshold stress σ_{thr} and true stress exponent n_t of the four alloys.

No.	Materials	n	σ_{thr}/ MPa	n_t
1	NH-El21	5.2	18.5	4.3
2	H-El21	4.9	16.7	4.1
3	NH-El21A	5.8	26.0	4.3
4	H-El21A	5.1	28.7	3.7

Applying the σ_{thr} in **Eq. 4**, **Eq. 5** is then given as:

$$n_t = \left(\frac{\partial \ln \dot{\varepsilon}}{\partial \ln \sigma_{thr}}\right)_T \quad (5)$$

The values of n_t are in a range that fits the theoretical assumption of creep mechanisms [17, 25, 57]. The results of n_t are close to 4 for all these four alloys, which are slightly lower than n values (**Fig. 14** and **Table 3**). Athul et al. [57] suggested that the true stress exponent 4-5 is related to the dislocation climb mechanism. It is therefore concluded that the main controlling mechanism was dislocation climb when these four alloys were crept at 240 °C under a stress of 80-140 MPa.

4.2.2 Effects of high shearing on creep properties

The effects of high shearing on the creep properties of the investigated alloys can be discussed based on its influences on their microstructures. As aforementioned, after high shearing, two apparent microstructural changes can be summarized. One is the grain coarsening. Another is that the intermetallics become dendritic and their distribution is denser. The influences from grain size could be negligible since the dominant creep mechanism is dislocation climb instead of grain boundary sliding (**Fig. 14**). Thus, in this section, the influence of high shearing on creep properties is discussed with focus on its effect on the intermetallic microstructure. Since Mg_3RE phase is the dominant intermetallic in both alloys, it is reasonable to conclude that the different creep resistance is related to the dendritic boundary strengthening caused by these Mg_3RE intermetallics phases. H-El21A alloy has the most pronounced dendritic structure of intermetallic among these four alloys (**Fig. 4**). These intermetallics not only distribute along α-Mg grain boundaries but also inside α-Mg grains. Mg_3RE phase, which is a thermal stable phase with a high melting point of 780 °C [58], can give a better boundary strengthening at elevated temperature during creep. Amberger et al. [59] stated that a high interconnectivity and strong skeleton structure of intermetallics can effectively shield load from α-Mg matrix and therefore lead to a higher creep resistance. With the assistance of high shearing, H-El21A has a shorter DAS (56.2±1.6 μm) than NH-El21A (74.0±6.4 μm), which exhibits a denser distribution of intermetallic phase in the α-Mg interiors. Consequently, more dendritic boundaries were covered by Mg_3RE phase to give a stronger resistance and more efficient dislocation impedance. Therefore, its creep resistance exhibits about one order of magnitude higher than that of NH-El21 and H-El21.

4.2.3 Effect of Al addition on creep properties

The present investigation discussed that the addition of 0.25% Al in El21 alloy creates a constitutional supercooling ahead of the solid/liquid interface and results in a dendritic morphology of α-Mg (**Fig. 2**(a) and (c)). Consequently, the morphology of intermetallic Mg_3RE was modified. Meanwhile, by adding Al, the formation of Al-Zr and Al-RE second phases were observed in NH-El21A and H-El21A alloys. Although their amount is not so high, their existence contributes to the improvement in creep resistance of Al-containing El21 alloys. Kabirian et al. [16] found that the creep resistance of the Zr-containing AZ91 alloy was enhanced due to the presence of Al_2Zr and Al_3Zr_2 intermetallics. Since Al_2Zr_3 and Al_2Zr phases were observed inside the grains in NH-El21A and H-El21A alloys, it is reasonable to conclude that the present Al_2Zr and Al_2Zr_3 phase can also act as obstacles to dislocations movement at elevated temperatures. Al_2Zr_3 phase is a high temperature phase, which is formed by peritectic reactions as following: $L + Al_4Zr_5 \leftrightarrow Al_2Zr_3$ at 1751 °C [37]. As for Al_2Zr phase in H-El21A with high shearing, its homogeneous distribution can give efficient resistance to hinder the dislocation movement. Besides the Al-Zr phases, with Al addition an additional Al_2Nd phase with small amount was formed in H-El21A alloy (**Fig. 9**). With the assistance of HSDT, the reaction of Al with RE was enhanced in H-El21A. Some of Al_2Nd particles filled the gap of the network Mg_3RE phase and made these intermetallics interconnected (**Fig. 9**(d-f)). They could supply additional resistance to impede the grain boundary sliding. Meanwhile, Al_2Nd has a higher melting temperature (1200 °C) than Mg_3RE [58], its existence may provide more efficient strengthening than Mg_3RE at elevated temperatures during creep. As a result, H-El21A alloy exhibits superior creep resistance to NH-El21A alloy. Zhang et al. [13] also verified that the creep resistance of AE41 alloy was enhanced by the occurrence of Al_2RE compound, which can inhibit the climbing of dislocation and the sliding and diffusion of grain boundary.

5. Conclusions

The influence from the addition of 0.25% Al and the employment of HSDT on the creep resistance of El21 alloy was investigated systematically. The following conclusions can be drawn:

1. The creep resistance of El21 alloy is significantly improved by about one order of magnitude with the combination of 0.25% Al addition and HSDT under all the applied stresses at 240 °C.

2. The grains of NH-El21A and H-El21A are coarsened due to the loss of grain refiner Zr by its chemical reaction with Al. The morphological transformation of intermetallics from equiaxed to dendritic derives from the solute segregation power of Al, which results in a significant constitutional supercooling ahead of solid/liquid interface.
3. HSDT is beneficial to break up the clusters of Al-Zr phase and change the Al-Zr compound from Al_2Zr_3 in NH-El21A alloy to Al_2Zr in H-El21A alloy. In addition, a small amount of Al_2Nd phase is formed due to the employment of HSDT in H-El21A alloy.
4. The dominant mechanism is dislocation climb during creep at elevated temperature 240 °C. The superior creep resistance of H-El21A alloy is mainly attributed to the dendritic and denser Mg_3RE intermetallic. They can effectively hinder the grain boundary sliding and dislocation movement. In addition, the formation of Al_2Zr phase and Al_2Nd with a high melting point can also act as an efficient obstacle to inhibit the dislocation movement, thus contributing to the improvement of creep resistance for H-El21A alloy.

Acknowledgements

The authors acknowledge Mr. G. Meister and Mr. Yiming Jin for preparing the alloys and Prof. Florian Pyczak and Mr. Uwe Lorenz for extending their TEM facilities. Hong Yang gratefully thanks the China Scholarship Council (201606050110) for the award of a fellowship and funding.

Reference

[1] B.L. Mordike, T. Ebert, Magnesium: Properties — applications — potential, Mater. Sci. Eng., A 302(1) (2001) 37-45.
[2] M. Celikin, Creep resistance in magnesium alloys Int. Mater. Rev. 55(4) (2010) 197-217.
[3] Y. Jin, C. Blawert, F. Feyerabend, J. Bohlen, M. Silva Campos, S. Gavras, B. Wiese, D. Mei, M. Deng, H. Yang, R. Willumeit-Römer, Time-sequential corrosion behaviour observation of micro-alloyed Mg-0.5Zn-0.2Ca alloy via a quasi-in situ approach, Corros. Sci. (2019) 108096.
[4] N. Mo, Q. Tan, M. Bermingham, Y. Huang, H. Dieringa, N. Hort, M.-X. Zhang, Current development of creep-resistant magnesium cast alloys: A review, Mater. Des. 155 (2018) 422-442.
[5] L. Liu, X. Chen, J. Wang, L. Qiao, S. Gao, K. Song, C. Zhao, X. Liu, D. Zhao, F. Pan, Effects of Y and Zn additions on electrical conductivity and electromagnetic shielding effectiveness of Mg-Y-Zn alloys, J. Mater. Sci. Technol. 35(6) (2019) 1074-1080.
[6] L. Liu, X. Chen, F. Pan, A. Tang, X. Wang, J. Liu, S. Gao, Microstructure, texture, mechanical properties and electromagnetic shielding effectiveness of Mg–Zn–Zr–Ce alloys, Mater. Sci. Eng., A 669 (2016) 259-268.

[7] X. Chen, L. Liu, F. Pan, J. Mao, X. Xu, T. Yan, Microstructure, electromagnetic shielding effectiveness and mechanical properties of Mg–Zn–Cu–Zr alloys, Mater. Sci. Eng., B 197 (2015) 67-74.
[8] J.R. TerBush, N.D. Saddock, J.W. Jones, T.M. Pollock, Partitioning of solute to the primary α-Mg phase in creep-resistant Mg-Al-Ca–based cast alloys, Metall. Mater. Trans. A 41(9) (2010) 2435-2442.
[9] A. Viswanath, H. Dieringa, K.K. Ajith Kumar, U.T.S. Pillai, B.C. Pai, Investigation on mechanical properties and creep behavior of stir cast AZ91-SiCp composites, J. Magnesium Alloys 3(1) (2015) 16-22.
[10] S.R. Agnew, K.C. Liu, E.A. Kenik, S. Viswanathan, Tensile and compressive creep behavior of die cast magnesium alloy AM60B, TMS Annu. Meet., 2000, pp. 285-290.
[11] S.M. Zhu, M.A. Gibson, M.A. Easton, J.F. Nie, The relationship between microstructure and creep resistance in die-cast magnesium–rare earth alloys, Scripta Mater. 63(7) (2010) 698-703.
[12] M. Suzuki, H. Sato, K. Maruyama, H. Oikawa, Creep behavior and deformation microstructures of Mg–Y alloys at 550 K, Mater. Sci. Eng., A 252(2) (1998) 248-255.
[13] Y. Zhang, L. Yang, J. Dai, J. Ge, G. Guo, Z. Liu, Effect of Ca and Sr on the compressive creep behavior of Mg–4Al–RE based magnesium alloys, Mater. Des. 63 (2014) 439-445.
[14] H. Dieringa, N. Hort, K.U. Kainer, Investigation of minimum creep rates and stress exponents calculated from tensile and compressive creep data of magnesium alloy AE42, Mater. Sci. Eng., A 510-511 (2009) 382-386.
[15] S. Zhu, M.A. Easton, T.B. Abbott, M.A. Gibson, J.-F. Nie, The influence of individual rare earth elements (La, Ce, or Nd) on creep resistance of die-cast magnesium alloy AE44 Adv. Eng. Mater. 18(6) (2016) 932-937.
[16] F. Kabirian, R. Mahmudi, Effects of Zr additions on the microstructure and impression creep behavior of AZ91 magnesium alloy, Metall. Mater. Trans. A 41(13) (2010) 3488-3498.
[17] L. Katsarou, M. Mounib, W. Lefebvre, S. Vorozhtsov, M. Pavese, C. Badini, J.M. Molina-Aldareguia, C.C. Jimenez, M.T. Pérez Prado, H. Dieringa, Microstructure, mechanical properties and creep of magnesium alloy Elektron21 reinforced with AlN nanoparticles by ultrasound-assisted stirring, Mater. Sci. Eng., A 659 (2016) 84-92.
[18] R. Daudin, S. Terzi, C. Mallmann, R.S. Martín, P. Lhuissier, E. Boller, A. Pacureanu, L. Katsarou, H. Dieringa, L. Salvo, Indirect improvement of high temperature mechanical properties of a Mg-based alloy Elektron21 by addition of AlN nanoparticles, Mater. Sci. Eng., A 688 (2017) 76-82.
[19] J. Zhao, K. Yu, X. Xue, D. Mao, J. Li, Effects of ultrasonic treatment on the tensile properties and microstructure of twin roll casting Mg–3%Al–1%Zn–0.8%Ce–0.3%Mn (wt%) alloy strips, J. Alloys Compd. 509(34) (2011) 8607-8613.
[20] J.B. Patel, X. Yang, C.L. Mendis, Z. Fan, Melt conditioning of light metals by application of high shear for improved microstructure and defect control, JOM 69(6) (2017) 1071-1076.
[21] G.-l. Zhu, J. Xu, Z.-f. Zhang, G.-j. Liu, Z. Fan, Effect of high shear rate on solidification microstructure of semisolid AZ91D alloy, Trans. Nonferrous Met. Soc. China 20 (2010) s868-s872.
[22] Z. Fan, G. Liu, Solidification behaviour of AZ91D alloy under intensive forced convection in the RDC process, Acta Mater. 53(16) (2005) 4345-4357.
[23] H. Men, B. Jiang, Z. Fan, Mechanisms of grain refinement by intensive shearing of AZ91 alloy melt, Acta Mater. 58(19) (2010) 6526-6534.
[24] Z. Fan, Y. Wang, M. Xia, S. Arumuganathar, Enhanced heterogeneous nucleation in AZ91D alloy by intensive melt shearing, Acta Mater. 57(16) (2009) 4891-4901.
[25] H. Yang, Y. Huang, B. Song, K.U. Kainer, H. Dieringa, Enhancing the creep resistance of AlN/Al nanoparticles reinforced Mg-2.85Nd-0.92Gd-0.41Zr-0.29Zn alloy by a high shear dispersion technique, Mater. Sci. Eng., A 755 (2019) 18-27.
[26] ASTM E112-13, Standard test methods for determining average grain size, ASTM International, West Conshohocken, PA, 2013.

[27] S.J. Liu, G.Y. Yang, S.F. Luo, W.Q. Jie, Microstructure evolution during heat treatment and mechanical properties of Mg–2.49Nd–1.82Gd–0.19Zn–0.4Zr cast alloy, Mater. Charact. 107 (2015) 334-342.
[28] L. Peng, P. Fu, Z. Li, Y. Wang, H. Jiang, High cycle fatigue properties of cast Mg–xNd–0.2Zn–Zr alloys, J. Mater. Sci. 49(20) (2014) 7105-7115.
[29] D. Wu, Y.Q. Ma, R.S. Chen, W. Ke, Effect of heat treatment on the microstructures and mechanical properties of the sand-cast Mg–2.7Nd–0.6Zn–0.5Zr alloy, J. Magnesium Alloys 2(1) (2014) 20-26.
[30] F. Wang, D.G. Eskin, A.V. Khvan, K.F. Starodub, J.J.H. Lim, M.G. Burke, T. Connolley, J. Mi, On the occurrence of a eutectic-type structure in solidification of Al-Zr alloys, Scripta Mater. 133 (2017) 75-78.
[31] X.-L. Yuan, D.-Q. Wei, Y. Cheng, G.-F. Ji, Q.-M. Zhang, Z.-Z. Gong, Pressure effects on elastic and thermodynamic properties of Zr_3Al intermetallic compound, Comput. Mater. Sci. 58 (2012) 125-130.
[32] V. Raghavan, Al-Cu-Zr (Aluminum-Copper-Zirconium), Journal of Phase Equilibria and Diffusion 32(5) (2011) 452-454.
[33] A. Laik, K. Bhanumurthy, G.B. Kale, Intermetallics in the Zr–Al diffusion zone, Intermetallics 12(1) (2004) 69-74.
[34] S.N. Agafonov, S.A. Krasikov, A.A. Ponomarenko, L.A. Ovchinnikova, Phase relations in the aluminothermic reduction of ZrO_2, Inorg. Mater. 48(8) (2012) 813-820.
[35] J. Dickson, L. Zhou, A. Paz y Puente, M. Fu, D.D. Keiser, Y.H. Sohn, Interdiffusion and reaction between Zr and Al alloys from 425° to 625°C, Intermetallics 49 (2014) 154-162.
[36] X. He, S. Yang, Y. Du, K. Tao, Y. Fan, Reaction layer formation at the interface between Ti or Zr and AlN, physica status solidi (a) 157(1) (1996) 99-106.
[37] R. Tamim, K. Mahdouk, Thermodynamic reassessment of the Al–Zr binary system, J. Therm. Anal. Calorim. 131(2) (2017) 1187-1200.
[38] S. Vummidi Lakshman, J.D. Gibbins, E.R. Wainwright, T.P. Weihs, The effect of chemical composition and milling conditions on composite microstructure and ignition thresholds of Al-Zr ball milled powders, Powder Technol. 343 (2019) 87-94.
[39] X. zheng, L. Wang, J. wang, Y. Wu, Z. Ning, J. Sun, L. Wang, Microstructure and mechanical properties of Mg–4Al–4Nd–0.5Zn–0.3Mn alloy, Mater. Sci. Eng., A 515(1) (2009) 98-101.
[40] M. Li, H. Hao, A. Zhang, Y. Song, X. Zhang, Effects of Nd on microstructure and mechanical properties of as-cast Mg-8Li-3Al alloy, J. Rare Earths 30(5) (2012) 492-496.
[41] M.S. Dargusch, S.M. Zhu, J.F. Nie, G.L. Dunlop, Microstructural analysis of the improved creep resistance of a die-cast magnesium–aluminium–rare earth alloy by strontium additions, Scripta Mater. 60(2) (2009) 116-119.
[42] J. Zhang, J. Wang, X. Qiu, D. Zhang, Z. Tian, X. Niu, D. Tang, J. Meng, Effect of Nd on the microstructure, mechanical properties and corrosion behavior of die-cast Mg–4Al-based alloy, J. Alloys Compd. 464(1-2) (2008) 556-564.
[43] S.M. Zhu, M.A. Gibson, J.F. Nie, M.A. Easton, T.B. Abbott, Microstructural analysis of the creep resistance of die-cast Mg–4Al–2RE alloy, Scripta Mater. 58(6) (2008) 477-480.
[44] A. Saboori, E. Padovano, M. Pavese, H. Dieringa, C. Badini, Effect of solution treatment on precipitation behaviors, age hardening response and creep properties of Elektron21 alloy reinforced by AlN nanoparticles, Materials 10(12) (2017) 1380.
[45] D.H. StJohn, M. Qian, M.A. Easton, P. Cao, Z. Hildebrand, Grain refinement of magnesium alloys, Metall. Mater. Trans. A 36(7) (2005) 1669-1679.
[46] M.A. Easton, D.H. StJohn, A model of grain refinement incorporating alloy constitution and potency of heterogeneous nucleant particles, Acta Mater. 49(10) (2001) 1867-1878.
[47] Y. Ali, D. Qiu, B. Jiang, F. Pan, M.-X. Zhang, Current research progress in grain refinement of cast magnesium alloys: A review article, J. Alloys Compd. 619 (2015) 639-651.
[48] Y. Jiang, Y.a. Chen, J. Gao, Comparative study regarding the effect of Al, Zn, and Gd on the microstructure and mechanical properties of Mg alloy Mg-Sn-Li, Mater. Des. 105 (2016) 34-40.

[49] L. Ceschini, A. Morri, A. Morri, A. Gamberini, S. Messieri, Correlation between ultimate tensile strength and solidification microstructure for the sand cast A357 aluminium alloy, Mater. Des. 30(10) (2009) 4525-4531.
[50] J.M.A.P.a.J.P. Abriata, The AI-Zr (Aluminum-Zirconium) System, Phase Diagram Evaluations: Section II 13 (1992) 277-291.
[51] J.N.a.B. Eichler, Extension of Miedema's macroscopic atom model to the elements of group 16 (0, S, Se, Te, Po), Paul Scherrer Institut (2003) 196.
[52] A.R. Miedema, P.F. de Châtel, F.R. de Boer, Cohesion in alloys — fundamentals of a semi-empirical model, Physica B+C 100(1) (1980) 1-28.
[53] J. Dai, S. Shen, B. Jiang, J. Zhang, Q. Yang, Z. Jiang, H. Dong, F. Pan, Interfacial reaction in (Mg-37.5Al)/(Mg-6.7Nd) diffusion couples, Met. Mater. Int. 22(1) (2016) 1-6.
[54] S.M. Zhu, J.F. Nie, M.A. Gibson, M.A. Easton, P. Bakke, Microstructure and creep behavior of high-pressure die-cast magnesium alloy AE44, Metall. Mater. Trans. A 43(11) (2012) 4137-4144.
[55] A. Srinivasan, H. Dieringa, C.L. Mendis, Y. Huang, R. Rajesh Kumar, K.U. Kainer, N. Hort, Creep behavior of Mg–10Gd–xZn (x=2 and 6 wt%) alloys, Mater. Sci. Eng., A 649 (2016) 158-167.
[56] Y. Li, T.G. Langdon, A simple procedure for estimating threshold stresses in the creep of metal matrix conposites, Scripta Mater. 36 (1997) 1457-1460.
[57] K.R. Athul, U.T.S. Pillai, A. Srinivasan, B.C. Pai, A review of different creep mechanisms in Mg alloys based on stress exponent and activation energy, Adv. Eng. Mater. 18(5) (2016) 770-794.
[58] N. Hort, Y. Huang, K.U. Kainer, Intermetallics in magnesium alloys, Adv. Eng. Mater. 8(4) (2006) 235-240.
[59] D. Amberger, P. Eisenlohr, M. Göken, On the importance of a connected hard-phase skeleton for the creep resistance of Mg alloys, Acta Mater. 60(5) (2012) 2277-2289.